In-situ X-ray microtomography of interface between additively manufactured aluminium bronze and H13 tool steel

In-situ X-ray microtomography of interface between additively manufactured aluminium bronze and H13 tool steel

Håkon Linga[1], Yubin Zhang[2], Vegard Brøtan[3], Xiaobo Ren[4], Ida Westermann[1] and Bjørn Holmedal[1]

[1] Department of Materials Science and Engineering, Norwegian University of Science and Technology, Sem Sælands vei 14, 7034, Trondheim, Norway.
[2] Department of Civil and Mechanical Engineering, Technical University of Denmark, Produktionstorvet, 425, 2800 Kgs. Lyngby, Denmark.
[3] SINTEF Manufacturing AS, S.P. Andersens vei 3, 7031, Trondheim, Norway.
[4] SINTEF Industry, Richard Birkelandsvei 2B, N-7465 Trondheim, Norway

E-mail: hakon.linga@ntnu.no

Abstract. Directed energy deposition (DED) is an additive manufacturing process category where material is melted as it is deposited, often powder melted with a focused laser. In this work aluminium bronze was deposited onto H13 tool steel using this technique, forming a mixing zone between the two metals. This mixing zone was examined with X-ray microtomography to obtain a three dimensional perspective that is unrealizable with conventional microscopy. Both the shape of the melt pools, the microstructure within, and processing defects could be discerned due to varying absorption of the radiation. In addition to characterizing the microstructure, the sample was also strained in three steps; the first step was to approximately 2.5 % strain, the second to 10.5 % and finally until fracture of the sample. The sample was scanned between each step, including a scan of the fracture surface. The ultimate tensile strength was found to be approximately 850 MPa and the fracture was observed to originate from cracks between the H13 substrate and the mixing zone. These cracks appeared to form in the second step of the straining. Additionally, local strains were estimated by utilizing pores in the sample as tracking points.

1. Introduction

Additive manufacturing (AM) allows combinations of different metals and alloys in the same part, which is difficult to achieve in more traditional production methods such as welding or casting. Uses for such multi-material solutions are abundant, but in general the idea is to utilize distinct properties for each material. One example is to use steel for its strength or wear resistance, while using copper or its various alloys for thermal- or corrosion properties. An application could be in injection moulding of plastic where thermal conduction is highly important in addition to a need for wear resistance in the tools[1]. Several studies have been done on deposition of copper on steels, but many of them focus on hardness or wear rate, and not on the adhesion between the metals[2, 3]. In this work, aluminium bronze deposited onto H13 tool steel is examined with X-ray microtomography, with gradually increasing loads. The motivation of using X-ray microtomography for additively manufactured parts is that it can

give a three-dimensional view on defects such as lack of fusion and pores[4]. Both types of defects are distinguishable with this technique, as voids results in lower absorption of radiation. Additionally, the mixing areas between metals are often anisotropic and complex so it is difficult to get a full understanding of the microstructure and its impact on mechanical properties from micrographs alone.

2. Experiment

The sample was made by first producing a block of H13 tool steel from powder with a composition of 5.40 wt% Cr, 0.38 wt% C, 1.38 wt% Mo, 1.18 wt% Si, 1.09 wt% V, 0.41 wt% Mn and Fe as balance. This was deposited by a laser with spot size of 1000 μm at a power of 500 W. 5 grams of powder was fed per minute, with a deposition speed of 1000 mm/min. After this, aluminium bronze powder with 8.5-10.75 wt% Al, 0.5-2.0 wt% Fe and Cu as balance was deposited onto the H13 steel with a laser spot size of 800 μm at 500 W, 3.8 grams of powder/minute and a laser speed of 1000 mm/min. A bi-directional laser scanning pattern was used throughout the build. The mixing zone between the two alloys was formed where the deposition of aluminium bronze remelted the previously deposited steel. From the as-built block a small tensile test sample, with a cross section of 0.5 x 1.0 mm and a gauge length of 1.25 mm, was made with electric discharge machining. This sample consisted of approximately 0.1 mm of aluminium bronze and a thin layer of H13 with a mixing zone in between the two alloys. The mixing zone with a thickness of 0.3 - 0.4 mm was roughly at the center of the gauge volume and parallel to the loading direction, as shown in Figure 1 a) and d). It would be sensible to have the interface perpendicular to the loading direction to test the strength here, but this could be problematic as it would be possible for the bronze to fail before the mixing zone[5]. This is also reinforced by preliminary microhardness results that show a hardness of approximately 500 HV3 in the bulk H13, 170 HV3 in the bulk aluminium bronze, and around 230 HV3 in the mixing zone, meaning that the bulk aluminium bronze should be the weakest part.

The absorption contrast was recorded with ZEISS Xradia 520 Versa, at 20 seconds exposure time at 3000 incident angles. The source to sample distance was 18 mm, while the sample to detector distance was 80 mm. An optical magnification of 4x was used, and the detector was set to a binning of 2. The reconstructed volume had a voxel size of 1.24 µm. Between scanning the sample, the sample was strained with a crosshead speed of $2 \cdot 10^{-3} \mathrm{mms}^{-1}$ using a specially designed rig [6]. While the sample was strained, applied force was recorded and closely monitored.

3. Results

Figure 1 a) shows the tensile test specimen prior to straining. The sample contains a region with aluminium bronze, a small region of H13 tool steel, and around half of the samples volume consists of the mixing zone between the two alloys. An example slice from the unstrained volume is displayed in Figure 1 d), while Figure 1 c) shows an optical micrograph within the mixing zone etched with Murakami's etchant. The mixing zone mainly consists of spherical iron particles suspended in the aluminium bronze. However, only larger particles can be clearly distinguished in the CT data, as seen in Figure 1 d). The line deposition direction refers to the direction of the deposition tracks of the mixing layer. The contour of these tracks of previous melt pools can be observed by the collection of iron particles along the two diagonal lines in Figure 1 d).

The samples were strained to fracture through three loading steps and the last load step corresponds to fracture. In the first two straining steps the engineering strain was estimated by measuring the change in distance between selected pores in opposite ends of the scanned volume. The loading data from the experiment is shown in Figure 1 b), where each strain step is separated by a dashed vertical line. Since the sample was analyzed with x-ray microtomography in between strain steps, approximately a day passed between each straining step. This time is

not shown in Figure 1 b). Additionally, some small pauses were done in the first straining step, and are the cause of the discontinuity in the plot around 50 to 60 seconds. The engineering strain along the loading axis was estimated to be around 2.5 % and 10.5 % in the first and second steps, respectively. The ultimate tensile strength was approximately 850 MPa.

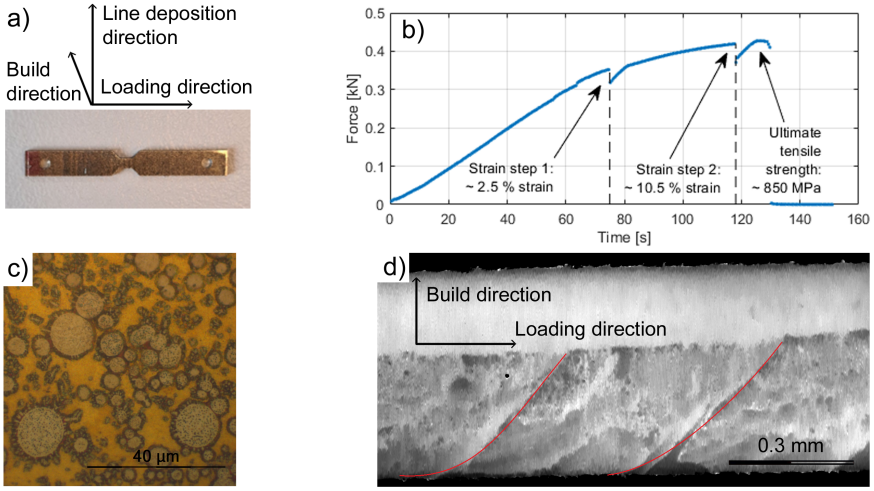

Figure 1. a) Tensile test specimen. b) Applied load plotted against time. c) Optical micrograph from the mixing zone. d) A slice from the unstrained volume. Red lines show melt pool contours.

By visual inspection the microstructure does not change much between straining steps; the iron particles can be observed in the same relative locations. However, pores are observed to emerge and grow in size as shown in Figure 2. This shows minimum intensity projections, where the minimum recorded absorption of the X-rays into the plane are displayed. The lowest intensity comes from pores in the material, so all pores throughout the sample are presented. To get a more complete view, the projection is shown at three different angles, along the loading direction, 45° rotated about the build direction, and along the line deposition direction in the mixing zone. The contour of the melt pool can clearly be seen from the projection along the line deposition direction, similarly to what can be seen in Figure 1 d), as particles of iron are accumulated here throughout the whole volume.

It should also be noted that the projections shown of the unstrained, 2.5 % strained, and 10.5 % strained sample were cropped to avoid any of the volume outside to interfere with the projection. This is not done in the fractured sample, as this approach would not allow the fracture surface to be revealed. Therefore the outside volume was instead detected and set to the maximum possible intensity. The apparent increase in pores around the fracture surface is therefore due to errors in detecting the fracture surface. The vertical lines show the corners of the volume that is projected.

Five different pores are marked in Figure 2. Pore 1 can very faintly be observed in the unstrained volume, but is clearly visible in the volume strained to 2.5 %. This pore continues to grow with increasing strains. Pores 2 and 3 are also seen in the previous volumes, but are only distinctly revealed in the volume strained to 10.5 %. All these contrast the behaviour of the majority of the pores that are already present from the unstrained volume, that do not seem to grow as the sample is strained. Pore 4 shows a crack that is formed when the sample is strained to 10.5 %. This does not appear at all in previous volumes, and closer inspection shows that the crack is positioned at an interface between the H13 steel and the aluminium bronze. This is seen in the large square in the bottom right corner of Figure 2, and is a slice from the volume where the crack observed from the projection is present. Pore 5 shows a similar formation of pores in

the material close to the contour of the melt pool, but is instead a series of smaller unconnected pores. It should be noted that the five pores shown here do not make an exhaustive list of pore formation with increasing strain in the volume and are only highlighted as examples.

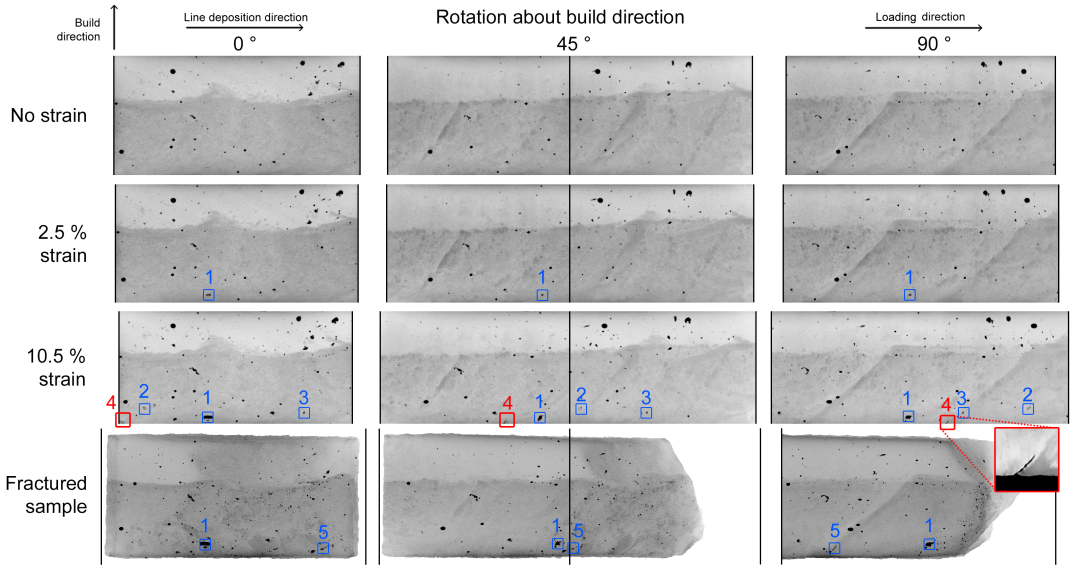

Figure 2. Minimum intensity projections at various strains and projection angles.

Closer examination of the location of the crack shown in Figure 2 reveals that the crack is not only positioned close to the contour of the melt pool, but is also aligned with the fracture surface. This can be observed better in Figure 3 a). The fracture surface is shown as a white line overlaid with slices from the volume strained to 10.5 %. The fracture surface is shown to closely follow the contour of the melt pool in some areas, but deviates from this contour and follows nearby pores in other areas as shown in Figure 3 b). However, a general observation is that the fracture initially follows the interface between the steel and bronze before deviating, as seen in Figure 3 c).

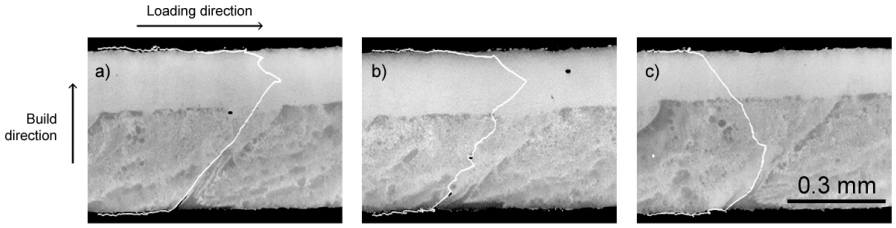

Figure 3. Fracture surface shown as white line overlapped with slices from the 10.5 % strained volume.

To further understand the plastic deformation behavior, the local strains were analyzed using pores as markers. The spatial coordinates were found for pores in both the unstrained and 10.5 % strained volumes. A selection of 80 out of around 250 pores were manually verified to be identical between the two volumes and were used to create a mesh using Delaunay triangulation. This resulted in just over 400 tetrahedrons with an average vertex distance of approximately 140 µm. The four vertexes in each tetrahedron were used to estimate the deformation gradient tensor, and from this the Green-Lagrange strain was found and placed in the incenter of each

tetrahedron. Figure 3 a) displays the normal strains compared to the location along the build direction and shows uniform strain with some local deviations throughout the build. In Figure 3 b) the axial strain is plotted against the radius ratio of the tetrahedrons. R is the radius of the circumscribed sphere and r is the radius of the inscribed sphere of the tetrahedrons, meaning an equilateral tetrahedron has a radius ratio of one[7]. An increased variance in axial strain is observed with decreasing radius ratio. The shear strains were also found, with an uniform distribution around zero with some small local variations.

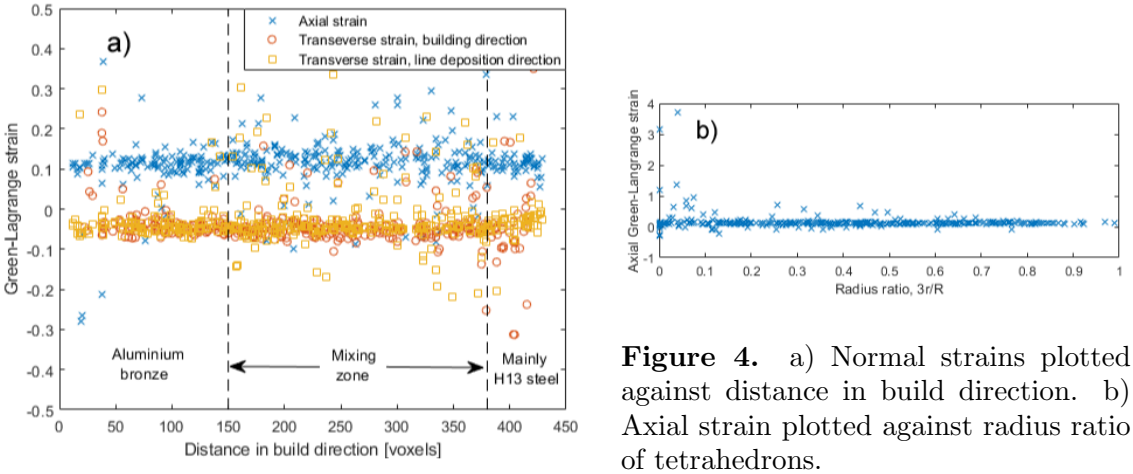

Figure 4. a) Normal strains plotted against distance in build direction. b) Axial strain plotted against radius ratio of tetrahedrons.

4. Discussion

The calculations done shows that the local strains were almost uniform throughout the sample with some local variations. There could be several reasons for these local strain variations. The first is related to the local microstructural variation, where one could envision variation depending on location within the melt pools in addition to variation along the building direction, where the local composition changes considerably. Such correlation could however not be observed, but is likely due to the large average tetrahedron size. An alternative explanation of the observed variation in strain is that it originates from inaccuracies in the calculation of the strain. This could come from two different errors. The first is faults in the meshing. The pores can have very irregular spacing, making the Delaunay triangulation occasionally create tetrahedrons with sharp angles. This makes even exceedingly small errors in localizing the pore coordinates cause large errors in the calculated strains. This is confirmed in Figure 3 c), where the largest deviations are observed at low radius ratios, and thus unfavorably shaped tetrahedrons. The second type of possible error is shifting of indexed coordinate due to pore growth. As seen in Figure 2, some pores grow in size with increasing strain, making this a possible source of deviation. However, the growth of certain pores but not others suggests that the strain is not uniform. A finer mesh of tracked points would make the correlation between strain and microstructure clearer, and using a larger fraction of the pores would certainly be a step in the right direction.

Another possibility for improving both the accuracy and the resolution of the local strain calculations is to use the iron particles as tracking points. These are decidedly more abundant in the volume than pores, and more tracking nodes would allow a finer mesh. Digital volume correlation is an alternative method of calculating local strains[8]. This would eliminate the need of identifying and matching individual pores and particles in the microstructure, since this is based only on intensity variation. More work will be done along these lines to refine the strain calculation and to relate them with local microstructure.

When it comes to the subject of the crack formation shown in Figure 2, it is evident that pore 4 is in fact the initiation point, considering how perfectly it aligns with the fracture surface. However, one could argue that in a real scenario more of the H13 steel substrate would be used, and that the crack could simply be a result of surface imperfections. This could very well be the case, but either way large interfaces between H13 steel and aluminium bronze are weak compared to the rest of the material. This is evident from the fracture consistently aligning with this interface, even far away from the fracture initiation position. One possibility is that the crack could be a result of lack of fusion between the two metals. However, this is improbable as the boundary would in that case have a lower absorption due to a small gap between the metals. This would be present already in the unstrained volume. Although this cannot be observed here, it is plausible that the resolution is not high enough to discern it. Since the mixing zone is formed by rapid cooling after the powder is melted, high thermal stresses are also expected. Therefore it is not unlikely that residual stress built at the bronze-steel interface contributes to the failure.

5. Conclusions

The ultimate tensile strength of the aluminium bronze - H13 tool steel sample tested was approximately 850 MPa, and the axial engineering strain just prior to fracture was estimated to around 10.5 %. The local strain calculated from displacement of pores in the material showed similar results. Both the normal- and shear strains were close to uniform throughout the volume, independent on microstructural features. Some pores are shown to grow in size with increasing levels of strain, while others are seemingly unaffected and remain approximately the same size. A correlation between pore growth and local strain could however not be established. The fracture is likely to have been initialized in a crack that formed in an interface between H13 steel and aluminium bronze in the sample surface. Furthermore the crack is shown to propagate in interfaces between the two metals in addition to passing nearby pores. For further improvement of the fracture toughness in the mixing zone between aluminium bronze and H13 tool steel, the deposition parameters need to be optimized such that the segregation of iron along melt pool edges is reduced.

Acknowledgments

This research is based on the research activites within the center for research-based innovation, SFI Manufacturing in Norway and is partially funded by the Research Council of Norway (NFR) under contract number 237900. A special thanks to Nordic Additive Manufacturing AS and the national research project IPN NextMoldMaker hosted by Skriverform AS (Project No.: 281967, NFR) that have contributed with test parts, case description and AM parameter development. YZ acknowledges the support from the European Research Council (M4D ERC grant agreement, project number 788567).

References

[1] Wang Y, Gao Y, Li Y, Zhai W, Sun L and Zhang C 2019 *Emerg. Mater. Res.* **8** 538–51
[2] Schmidt M, Kolleck R, Grimm A, Veit R and Bartkowiak K 2010 *CIRP Ann. Manuf. Technol.* **59** 211–4
[3] Samodurova M, Shaburova N, Radionova L, Zakirov R, Pashkeev K, Myasoedov V, Erdakov I and Trofimov E 2020 *Mater.* **13** 461–71
[4] Sames W, Medina F, Peter W, Babu S and Dehoff R 2014 *Effect of Process Control and Powder Quality on Inconel 718 Produced Using Electron Beam Melting* (John Wiley & Sons, Ltd) pp 409–23
[5] Liu L, Zhuang Z, Liu F and Zhu M 2013 *Int. J. Adv. Manuf. Technol.* **69** 2131–2137
[6] Kobayashi M, Zhang Y, Ishikawa H, Sun J, Oddershede J, Jensen D and Miura H 2021 *Exp. Mech.* **61** 817–28
[7] Liu A and Joe B 1994 *BIT Numer. Math.* **34** 268–87
[8] Xu C, Andriollo T, Zhang Y, Hernando J, Hattel J and Tiedje N 2020 *Scr. Mater.* **178** 463–7